Development of reduced and optimized reaction mechanism for potassium emissions during pulverized-biomass combustion based on genetic algorithms

Kaidi Wan[a,b,*], Luc Vervisch[c], Chongwen Jiang[a,b], Pascale Domingo[c], Zhenxun Gao[a,b], Jun Xia[e], Zhihua Wang[d]

[a]*Aircraft and Propulsion Laboratory, Ningbo Institute of Technology, Beihang University, Ningbo 315832, China*
[b]*National Laboratory for Computational Fluid Dynamics, School of Aeronautic Science and Engineering, Beihang University, Beijing 100191, China*
[c]*CORIA – CNRS, Normandie Université, INSA de Rouen, 76801 Saint-Etienne-du-Rouvray, France*
[d]*State Key Laboratory of Clean Energy Utilization, Zhejiang University, Hangzhou 310027, China*
[e]*Department of Mechanical and Aerospace Engineering & Institute of Energy Futures, Brunel University London, Uxbridge UB8 3PH, UK*

Abstract

A reduced mechanism for potassium chemistry under combustion conditions is derived from a detailed chemical mechanism for alkali metal emissions (Glarborg and Marshall, 2005), which could be useful for three-dimensional (3D) numerical simulations of potassium emissions by biomass combustion furnaces. An automated chemistry reduction and optimization approach relying on canonical micro-mixing problem is applied to develop the reduced mechanism, whose performance is then evaluated in two-dimensional (2D) carrier-phase direct numerical simulation (DNS) of pulverized-biomass combustion. Good agreements are achieved between predictions of the reduced and the detailed mechanisms on the four major potassium species, i.e., K, KOH, KCl and K_2SO_4. The prediction capabilities of the reduced mechanism for various K/Cl/S ratios in the volatiles are further investigated by a parametric study with 14 two-dimensional DNS cases. The potassium chemistry under those various conditions are predicted well by the reduced potassium mechanism with a CPU cost reduction reaching up to 71.3% compared to the detailed reference mechanism.

Keywords: Pulverized-biomass combustion, Direct numerical simulation, Potassium, Chemistry reduction, Genetic algorithm

1. Introduction

As a carbon neutral fuel, biomass resource is attracting more attention recently due to the urgent requirement of reducing CO_2 emissions to control global warming [1–3]. Nowadays, biomass and its thermal-conversion products, e.g. solid/liquid biofuels and biogases, already contribute 10% of the world total primary energy supply [4]. Biomass could substitute coal in most present coal-fired power plants without reconstruction, with a maximum mass ratio of biomass about 20–30% [5]. On the other hand, because of the relatively high alkali metal content in biomass, alkali-induced slagging issue becomes one of the most challenging problems in the practical thermo-utilization of biomass [6, 7], especially for herbaceous plants which are rich in potassium (K) [8]. During the combustion of biomass, alkali species can be released into gas phase and then condense on heat exchange surfaces of the furnace, which generates an initial sticky layer and then captures fly ash resulting in rapid ash deposition [9, 10]. Besides, fouling and corrosion issues are also found due to high chemical activity of chlorine and sulfur compounds of alkali, e.g., KCl [11]. These alkali-induced issues severely limit the clean and efficient utilization of biomass resources.

Over the past decades, experimental measurements on alkali chemistry during biomass combustion evolves from offline sampling to online laser diagnostics techniques [12–14]. The time-resolved alkali release process during the combustion can be directly captured by using the online laser techniques, e.g., tunable diode laser absorption spectroscopy (TDLAS) [15], and collinear photofragmentation and atomic absorption spectroscopy (CPFAAS) [16]. Recently, Liu et al. [17] applied planar laser-induced fluorescence (PLIF) and multi-point laser-induced breakdown spectroscopy (LIBS) methods to quantitatively measure the atomic and elemental potassium released from a burning biomass pellet. Weng et al. [18] measured the spatial distribution of potassium hydroxide (KOH) and potassium chloride (KCl) simultaneously around single burning pulverized biomass char particles by employing laser-induced photofragmentation fluorescence (LIPF) technique.

On the modeling side, one-step and two-step Arrhenius potassium release models have been developed for biomass pellet combustion by Zhang et al. [19] and Liu et al. [17], respectively.

*Corresponding author
Email address: wankaidi@buaa.edu.cn (Kaidi Wan)

These models are suitable to describe potassium release of biomass in typical circulating fluidized bed (CFB) combustion, as the diameter and burnout time of biomass in these studies are with the same order of magnitude of biomass fuel in a typical CFB boiler [20].

To describe the post-release alkali reaction dynamics during combustion, the first detailed alkali mechanisms were developed by Srinivasachar et al. [21] and Steinberg and Schofield [22]. Based on that, Glarborg and Marshall [23] proposed a detailed alkali mechanism encompassing the elements Na, K, C, H, O, S and Cl, and it was carefully validated against the experimental results of homogeneous sulfation of alkali chloride under combustion conditions [24]. However, the complexity of this reference detailed alkali mechanism [23], which includes 48 Na/K/O/H/Cl/S species and 202 elementary reactions, largely limits its application in computational fluid dynamic (CFD) simulations. Hence, in the literature the reported CFD simulations of real combustion systems with alkali reactions employed simplified versions of the detailed mechanism. Akbar et al. [25] employed a K/O/H/Cl subset with 14 reactions to predict the potassium reactions in a 0.5 MW pulverized-fuel combustion facility using Reynolds-Averaged Navier-Stokes (RANS) simulations. Garba et al. [26] developed a reduced mechanism containing 36 K/O/H/Cl/S species and 137 reactions using sensitivity analysis and applied it to RANS simulations of a 10 MW biomass-fired furnace. However, to the best of our knowledge, a systematic reduction study of the detailed alkali mechanism for biomass combustion has not been reported yet, which could potentially benefit the CFD investigations of biomass furnaces.

Within this context and considering only one alkali metal, K, for biomass combustion, the aim of the present study is twofold. First, a reduced potassium mechanism is developed from the detailed one by Glarborg and Marshall [23] using systematic chemistry reduction and rate optimization techniques [27, 28]. Second, the performance of the reduced mechanism is then carefully examined in two-dimensional (2D) direct numerical simulations (DNS) of pulverized-biomass combustion.

2. Automated reduction and optimization of potassium reaction kinetics

The potassium reaction dynamics during the combustion of biomass volatile is investigated. The volatile of corn straw [17] is employed, for which the chemical properties are shown in Table

Table 1: Properties of corn straw [10]

Proximate analysis (wt%)				Ultimate analysis (wt%)				
M_{ad}	A_{ad}	V_{ad}	FC_{ad}	C_{daf}	H_{daf}	N_{daf}	S_{daf}	O_{daf}
11.6	7.9	64.2	16.3	43.9	4.5	1.8	0.4	49.3

Ash analysis (wt%)							Cl_{ad}	K_{ad}
SiO_2	Al_2O_3	Fe_2O_3	CaO	MgO	K_2O	Na_2O	(mg/g)	(mg/g)
47.52	5.64	1.04	4.51	12.6	7.87	1.97	1.34	13.1

Table 2: Modeled volatile compositions of corn straw.

Hydrocarbon volatile compositions (mass fractions)					
CH_4	C_2H_2	CO	H_2	CO_2	H_2O
0.0322	0.1805	0.2536	0.0215	0.1853	0.3024

Non-hydrocarbon volatile compositions (mass fractions)		
KOH	HCl	SO_2
0.0147	0.0018	0.0080

1. The previously validated DRM22 mechanism proposed by Kazakov and Frenklach [29] is used to describe the hydrocarbon combustion of the volatile, which contains 22 chemical species and 104 elementary reactions. The compositions of the hydrocarbon volatile are preliminary determined via the bio-chemical percolation devolatilization (bio-CPD) model [30–32], with the Tar species replaced by C_2H_2 [33]. Then minor adjustments are applied to the compositions to fulfill the elemental mass conservation and the lower heating value of the corn straw [34]. The final volatile compositions are given in Table 2.

Following previous researches on sodium emissions by coal combustion [35], the initial potassium species in the volatile is set to be KOH, while those of S and Cl are set to be SO_2 and HCl, respectively. According to the experimental results [17], 58.1% of the mass of potassium present in the biomass is released during pyrolysis. However, no experimental information is available for the release of chlorine and sulfur. Here, they are assumed to follow the ratio of volatile yields during pyrolysis as predicted by the bio-CPD model, i.e., 87.3% of the mass of chlorine and sulfur is released along with the volatiles. The mass fractions of KOH, HCl and SO_2 in the volatile can then be computed, as summarized in Table 2.

The reactions of K/S/Cl species are simulated using the detailed mechanism by Glarborg and

Marshall [23] containing the elements Na, K, C, H, O, S and Cl. In this work, the element Na is not considered, which leads to a reference detailed mechanism of potassium reactions involving 35 species and 153 elementary reactions.

2.1. Stochastic micro-mixing problem

To develop a reduced potassium mechanism which can be applied under a wide range of conditions, a turbulent non-premixed micro-mixing based canonical problem is introduced as a reference problem for the reduction of the reference detailed mechanism. This approach has been detailed in Jaouen et al. [27], and only the core idea is given here.

Within a Lagrangian framework, the time evolution of the composition and energy of a traveling fluid particle can be computed with the diffusive budget described by a deterministic micro-mixing closure, as the linear relaxation model (IEM or LMSE) [36, 37]:

$$\frac{d\varphi^L(t)}{dt} = \frac{\langle\varphi\rangle(t) - \varphi^L(t)}{\tau_T} + \dot{\omega}_\varphi, \tag{1}$$

where φ is a thermochemical variable, i.e., species mass fractions and temperature, while $\langle\varphi\rangle$ is the mean flow condition seen by the traveling particles at a given time. $\dot{\omega}_\varphi$ is the chemical source of φ and τ_T is a characteristic turbulent mixing time. Solving for Eq. (1) starting from initial conditions, e.g., pure fuel, oxidizer or burnt gases, a trajectory $\varphi^L(t)$ can be obtained. The average mixture environment seen during the trajectory is characterized by [27]

$$\langle\varphi\rangle(t) = \frac{1}{N_p}\sum_{p=1}^{N_p}\varphi^p(t)\,, \tag{2}$$

where $\varphi^p(t)$ $(p = 1, \cdots, N_p)$ is a set of stochastic particles whose thermochemical properties evolve according to chemical reactions and a micro-mixing closure, here the well-known Curl closure [38] is employed. The time evolutions of those stochastic particles are solved aside from any simulation in physical space, to cover the range of the representative composition space of the flow problem under investigation. Initially, the N_p stochastic particles are divided into n_I groups, with n_I the number of inlets. The number of particles for each inlet is determined according to the relative

contribution of the inlet to the total mass flow rate of the flow problem. The particles assigned to a given inlet take the species composition and temperature of that inlet. In addition, some particles may be set with burnt gases conditions to secure ignition and/or mimic dilution by burnt gases. Then a deterministic trajectory $\varphi^L(t)$ can be computed from every inlet (Eq. 1). This micro-mixing based canonical approach of analyzing the response of reduced chemical mechanisms has been previously applied to a four inlets methane/vitiated-air/hydrogen-air/steam combustion system [27].

The operating conditions of the micro-mixing problem in the present study are those of the pulverized-biomass jet flame studied in [39], which are also adopted thereafter for DNS. Three inlet streams are involved, i.e., the oxidizer air, the fuel volatile and a high-temperature third inlet. The volatile composition (see Table 2) of corn straw is employed and the third inlet is the burnout gas of the volatile and air at $\phi = 0.45$. The mass flow rate of the three inlets, i.e., the number of particles per inlet, is chosen so that the overall system operates under the stoichiometric condition. In total 500 particles is employed, and 4% of them are initially set to the chemical equilibrium condition at $\phi = 1$, to secure ignition. The micro-mixing time τ_t is set to 0.2 ms, with a weak sensitivity of the obtained reduced mechanism to this parameter, as soon as its value allows for ignition (see [27] for a sensitivity analysis on τ_t).

The ORCh (Optimized and Reduced Chemistry) method, reported in detail in [27, 28] and previously employed for modeling meso-scale combustion [40] and selective non-catalytic reduction [41], is coupled with the CANTERA [42] chemical kinetics solver. ORCh consists of a combination of Directed Relation Graph with Error Propagation (DRGEP) [43, 44] analyses, to which a Genetic Algorithm (GA) [45] is added to optimize the chemical rates parameters of the reduced mechanism.

2.2. DRGEP

First, the species and elementary reactions which make a minor contribution to the stochastic micro-mixing problem are removed by the DRGEP approach. The details of DRGEP can be found in the seminal papers by Lu and Law [43] and Pepiot and Pitsch [44]. Here, only the main lines are given as follows.

First, a set of target species is defined, from the species which need to be predicted accurately by the reduced mechanism. Here, it includes the four major potassium species K, KOH, KCl and K_2SO_4. Then, species and reactions are automatically ordered according to their relative influence on the evolution of the target species listed above, which is obtained by comparing the variation rate of a target species when a non-target species or elementary reaction is involved against the total variation rate of that target species [44].

Starting from the least important one, the species and reactions are progressively removed from the detailed mechanism and the deterministic trajectory $\varphi_k^L(t_\ell; n)$ (Eq. 1) is re-computed after each removing operation. k denotes the k-th targeted thermochemical property ($k = 1, \cdots, N_t = 4$), t_ℓ is the ℓ-th point ($\ell = 1, \cdots, N_\ell = 1000$) of a chemical trajectory versus time, n denotes the n-th inlet ($n = 1, \cdots, N_I = 3$). The obtained distributions of $\varphi_k^L(t_\ell; n)$ of the target species mass fractions are compared against $\varphi_k^{\mathrm{Ref}}(t_\ell; n)$, and the error measure is calculated as:

$$E = \frac{1}{N_I \cdot N_t \cdot N_\ell} \sum_{n=1}^{N_I} \sum_{k=1}^{N_t} \sum_{\ell=1}^{N_\ell} \left| \frac{\varphi_k^{\mathrm{Ref}}(t_\ell; n) - \varphi_k^L(t_\ell; n)}{\varphi_k^{\mathrm{Ref}}(t_\ell; n)} \right|. \tag{3}$$

With the error threshold $E = 0.1\%$, 20 K/S/Cl species are removed during the DRGEP reduction, resulting in 15 K/S/Cl species. Then, the number of reactions is further downsized to 24 with $E = 0.96\%$ (Table 3, but using the original rates parameters from [23]).

During DRGEP, 7 elementary reactions are chosen as the most important ones over the original 23 reactions of the detailed mechanism for the K/C/H/O subsystem:

$$\mathrm{K + O_2\,(+M) \rightleftharpoons KO_2\,(+M)} \tag{R1}$$

$$\mathrm{H_2O + KO \rightleftharpoons KOH + OH} \tag{R2}$$

$$\mathrm{CO + KO \rightleftharpoons CO_2 + K} \tag{R3}$$

$$\mathrm{H + KOH \rightleftharpoons H_2O + K} \tag{R4}$$

$$\mathrm{2\,KOH \rightleftharpoons K_2O_2H_2} \tag{R5}$$

$$\mathrm{H + KO_2 \rightleftharpoons HO_2 + K} \tag{R6}$$

$$\mathrm{CO + KO_2 \rightleftharpoons CO_2 + KO} \tag{R7}$$

In this subsystem, the reactions between KOH and the radicals OH and H (R2, R4) are kept along with the equilibrium between KOH and $K_2O_2H_2$ (R5). KO_2 is formed via the three-body reaction

(R1) and reacts with radical H and CO (R6, R7). The reduction reaction of KO by CO is also kept (R3). In the K/H/O/Cl subsystem, 4 elementary reactions over the 10 original ones enter the reduced mechanism, which produce KCl from HCl and K (R8), KOH (R9) and KO_2 (R10) and secure the equilibrium between KCl and K_2Cl_2 (R11):

$$HCl + K \rightleftharpoons H + KCl \quad \text{(R8)}$$

$$HCl + KOH \rightleftharpoons H_2O + KCl \quad \text{(R9)}$$

$$HCl + KO_2 \rightleftharpoons HO_2 + KCl \quad \text{(R10)}$$

$$2\,KCl \rightleftharpoons K_2Cl_2 \quad \text{(R11)}$$

Over the 17 reactions of K/H/O/Cl/S subsystem, 7 are required by the reduced mechanism: 2 three-body reactions producing KSO_3 (R12, R13) and one producing $KHSO_4$ (R14); 3 reactions contribute to the formation of K_2SO_4 (R16, R17, R18); the reaction between KSO_3 and radical OH (R15).

$$K + SO_3\,(+M) \rightleftharpoons KSO_3\,(+M) \quad \text{(R12)}$$

$$KO + SO_2\,(+M) \rightleftharpoons KSO_3\,(+M) \quad \text{(R13)}$$

$$KOH + SO_3\,(+M) \rightleftharpoons KHSO_4\,(+M) \quad \text{(R14)}$$

$$KSO_3 + OH \rightleftharpoons KOH + SO_3 \quad \text{(R15)}$$

$$KO + KSO_3 \rightleftharpoons K_2SO_4 \quad \text{(R16)}$$

$$KHSO_4 + KOH \rightleftharpoons H_2O + K_2SO_4 \quad \text{(R17)}$$

$$KCl + KHSO_4 \rightleftharpoons HCl + K_2SO_4 \quad \text{(R18)}$$

4 elementary reactions driving the oxidation of sulfur containing species (R19 to R22) are included in the SO_2/SO_3 interconversion subsystem of the reduced mechanism:

$$HOSO_2 + O_2 \rightleftharpoons HO_2 + SO_3 \quad \text{(R19)}$$

$$O + SO_2\,(+M) \rightleftharpoons SO_3\,(+M) \quad \text{(R20)}$$

$$OH + SO_2\,(+M) \rightleftharpoons HOSO_2\,(+M) \quad \text{(R21)}$$

$$OH + SO_2 \rightleftharpoons H + SO_3 \quad \text{(R22)}$$

Finally, the H/O/Cl subsystem requires only one three-body (R23) and one replacement reactions (R24) in the reduced mechanism:

$$HCl + M \rightleftharpoons Cl + H + M \quad \text{(R23)}$$

$$HCl + OH \rightleftharpoons Cl + H_2O \quad \text{(R24)}$$

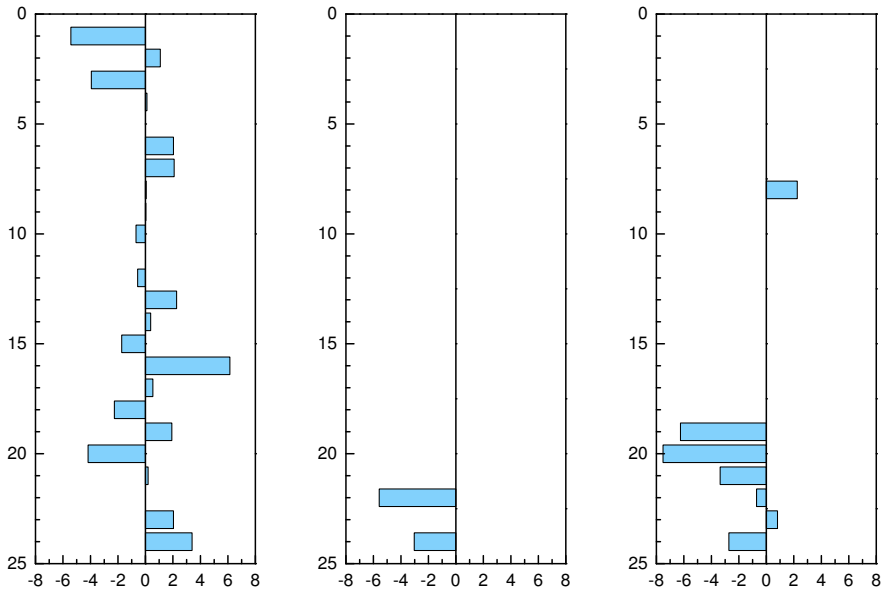
Table 3: The 15 K/S/Cl species and 24 reactions mechanism reduced by DRGEP and kinetic rates optimized by genetic algorithm over a stochastic micro-mixing problem. Units are mol, s, cm^3, cal and K. The Chaperon efficiencies of the reference mechanism [23] are preserved for both three-body and fall-off reactions. Electronic format available in the supplementary material.

	Reaction	A	β	E
1	$K + O_2 (+M) \rightleftharpoons KO_2 (+M)$	5.84e+13	0	0
2	$H_2O + KO \rightleftharpoons KOH + OH$	1.85e+14	0	0
3	$CO + KO \rightleftharpoons CO_2 + K$	2.81e+13	0	0
4	$H + KOH \rightleftharpoons H_2O + K$	5.17e+13	0	0
5	$2\,KOH \rightleftharpoons K_2O_2H_2$	8.00e+13	0	0
6	$H + KO_2 \rightleftharpoons HO_2 + K$	3.92e+14	0	0
7	$CO + KO_2 \rightleftharpoons CO_2 + KO$	1.96e+14	0	0
8	$HCl + K \rightleftharpoons H + KCl$	1.02e+14	0	3717
9	$HCl + KOH \rightleftharpoons H_2O + KCl$	1.72e+14	0	0
10	$HCl + KO_2 \rightleftharpoons HO_2 + KCl$	1.12e+14	0	0
11	$2\,KCl \rightleftharpoons K_2Cl_2$	8.00e+13	0	0
12	$K + SO_3 (+M) \rightleftharpoons KSO_3 (+M)$	8.32e+13	0	0
13	$KO + SO_2 (+M) \rightleftharpoons KSO_3 (+M)$	7.91e+14	0	0
14	$KOH + SO_3 (+M) \rightleftharpoons KHSO_4 (+M)$	1.13e+14	0	0
15	$KSO_3 + OH \rightleftharpoons KOH + SO_3$	1.18e+13	0	0
16	$KO + KSO_3 \rightleftharpoons K_2SO_4$	7.25e+14	0	0
17	$KHSO_4 + KOH \rightleftharpoons H_2O + K_2SO_4$	1.19e+14	0	0
18	$KCl + KHSO_4 \rightleftharpoons HCl + K_2SO_4$	4.83e+13	0	0
19	$HOSO_2 + O_2 \rightleftharpoons HO_2 + SO_3$	1.32e+12	0	615
20	$O + SO_2 (+M) \rightleftharpoons SO_3 (+M)$	1.34e+10	0	1563
21	$OH + SO_2 (+M) \rightleftharpoons HOSO_2 (+M)$	7.63e+12	0	691
22	$OH + SO_2 \rightleftharpoons H + SO_3$	4.90e+02	2.54	23681
23	$HCl + M \rightleftharpoons Cl + H + M$	8.36e+13	0	82417
24	$HCl + OH \rightleftharpoons Cl + H_2O$	4.83e+07	1.60	−214

2.3. Genetic algorithm

A genetic algorithm searches for the optimal solution of a problem by applying the principles of natural selection and evolution to an initialized population of potential solutions [45]. In the present work, genetic algorithm is employed to optimize the kinetic parameters of the reduced mechanism obtained via DRGEP, i.e., the pre-exponential factor A_j, the temperature exponent β_j, and the activation energy E_j. Here, $a_j = \log A_j$ is introduced to eliminate the effects of high values associated to A_j. A chromosome is constituted of a set of the three parameter values (a_j, β_j, E_j),

while each parameter value is a gene. A set of 48 chromosomes, i.e., the population of the genetic algorithm problem $M = 48$, is applied with an allowed variation of ±8% for each of the three chemical parameters. The kinetic rates of the resulting optimal reduced mechanism are given in Table 3. The corresponding relative variations of the chemical parameters of the elementary reactions are shown in % in Fig. 1.



(a) log(A) (b) β (c) E

Figure 1: Variation of the rate parameters of the reduced mechanism in % measured from the detailed reference mechanism [23]. Reactions are ordered as in Table 3.

Figures 2 and 3 show the evolutions of temperature and mass fractions of major species for the detailed mechanism [23], the optimized reduced mechanism of Table 3 and the preliminary reduced mechanism (DRGEP, Table 3 but with original rates parameters). The trajectories issued from fuel, oxidizer and the third coflow inlets are displayed. It can be observed that the hydrocarbon combustion is perfectly reproduced by the reduced mechanism (either with the optimized or the original rates parameters) and the ignition occurring around 0.5 ms is also well captured (Fig. 2). Indeed, the same DRM22 mechanism is employed to describe the hydrocarbon oxidation, combined with the detailed or the reduced mechanisms for potassium chemistry. Since the non-hydrocarbon components, i.e., K/Cl/S species, are minor in the volatile gas, the influence of

the potassium chemistry on the hydrocarbon combustion should be marginal.

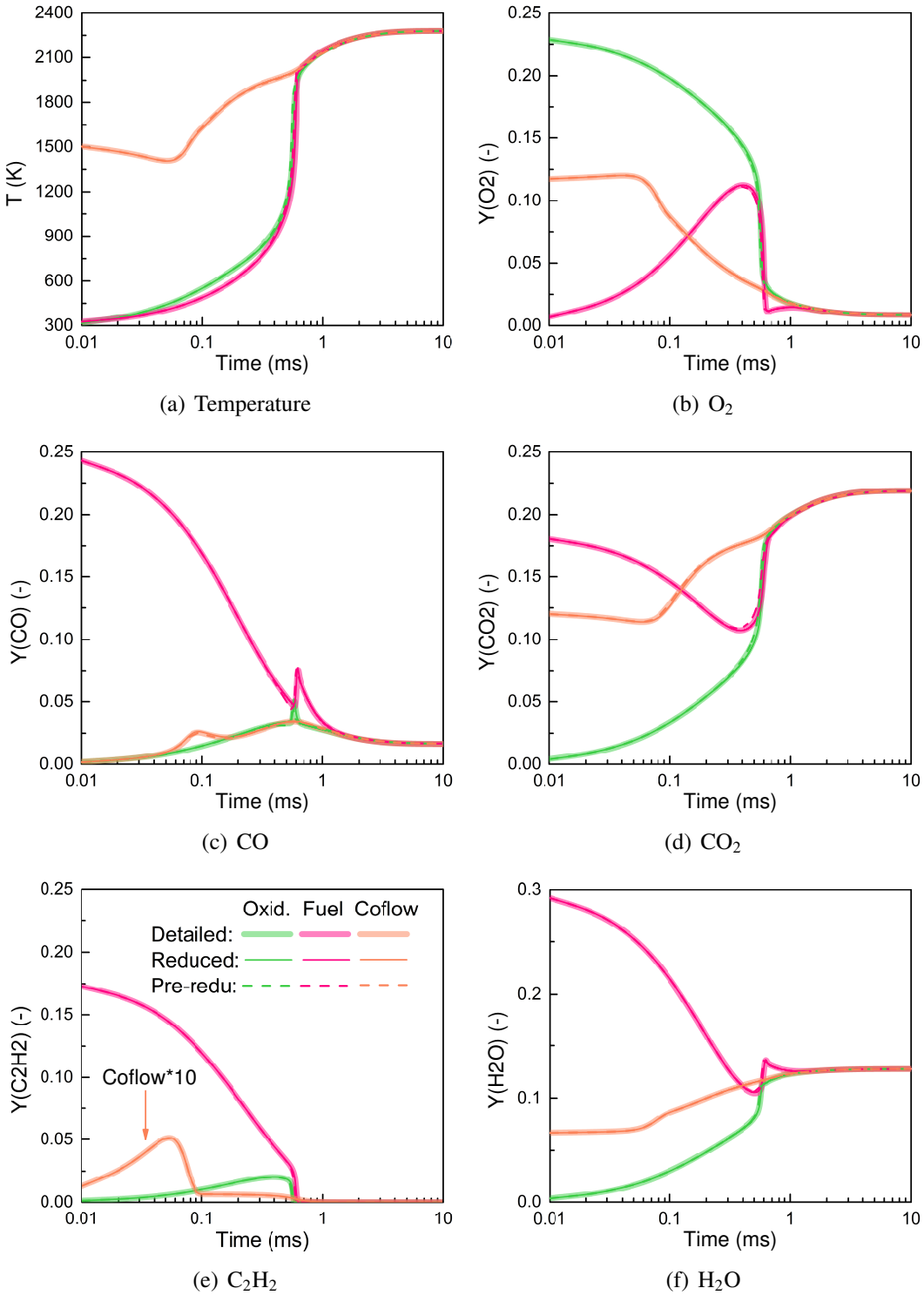
For the dynamics of potassium chemistry, all the four major potassium species reach their peak mass fractions around the ignition time, especially for the fuel trajectory (Fig. 3). This should be attributed to the production of radicals from the actively combustion process, which activates the potassium chemistry (see Table 3). Subject to random mixing, the radicals quench and the concentration of potassium species drops, to then slowly evolves towards the equilibrium. Comparing the results from the preliminary reduced mechanism based on the original rates parameters, the reduced mechanism with rates parameters optimized by the genetic algorithm shows a better agreement with the detailed reference, especially for the trajectories of K_2SO_4. As shown in Figs. 3(d) and 4, the predictions of reduced mechanism on K_2SO_4 are significantly improved when the optimized rates parameters are employed. It confirms the advantage in adding the optimization of the rate parameters by the genetic algorithm to better predict minor pollutant species, specifically considering the fact that the number of sulfur containing species has been heavily reduced by 73% from 22 to 6 by DRGEP.

Note that the presence of KCl in gaseous form at the beginning of fuel stream trajectory (Fig. 3(c)), is justified by the fact that once the chemical reactions are activated for the volatile fuel, KCl is produced at 300 K. First, $K_2O_2H_2$ is produced via $2\,KOH \rightleftharpoons K_2O_2H_2$. Second, KOH reacts with HCl in the volatile fuel by $KOH + HCl \rightleftharpoons KCl + H_2O$, and KCl subsequently forms K_2Cl_2 through $2\,KCl \rightleftharpoons K_2Cl_2$. In real biomass combustion, the potassium species should be in condensed form at low temperature and therefore the results in the unburned region of the canonical micro-mixing problem are questionable. However, this artifact hopefully disappears in the pulverized-biomass flames discussed thereafter, since the potassium is released along with volatile at a much higher temperature.

3. Evaluation of the reduced mechanism in 2D pulverized-biomass flame

3.1. DNS flow configuration

A two-dimensional direct numerical simulation (DNS) of a temporally evolving pulverized-biomass jet flame with potassium emission is now performed with the reduced mechanism (Fig.

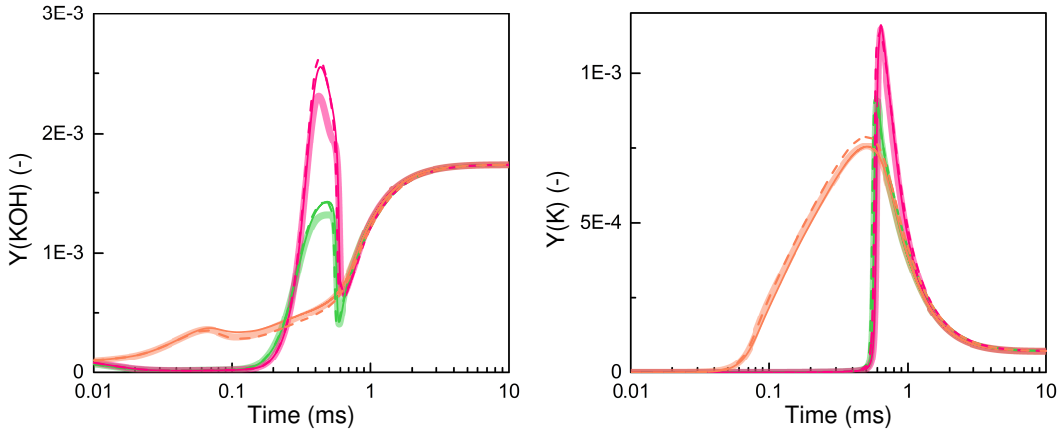


(a) Temperature (b) O_2

(c) CO (d) CO_2

(e) C_2H_2 (f) H_2O

Figure 2: Time evolution of the deterministic mixing trajectories (Eq. 1). Temperature and species mass fractions. Green: from oxidizer stream. Pink: fuel stream. Orange: coflow stream. Thick solid lines: detailed mechanism [23]. Thin solid lines: reduced mechanism (Table 3). Dashed lines: preliminary reduced mechanism (DRGEP, Table 3 but with original rates parameters)



(a) KOH (b) K

(c) KCl (d) K_2SO_4

Figure 3: Time evolution of the deterministic mixing trajectories (Eq. 1). Species mass fractions. Green: from oxidizer stream. Pink: fuel stream. Orange: coflow stream. Thick solid lines: detailed mechanism [23]. Thin solid lines: reduced mechanism (Table 3). Dashed lines: preliminary reduced mechanism (DRGEP, Table 3 but with original rates parameters)

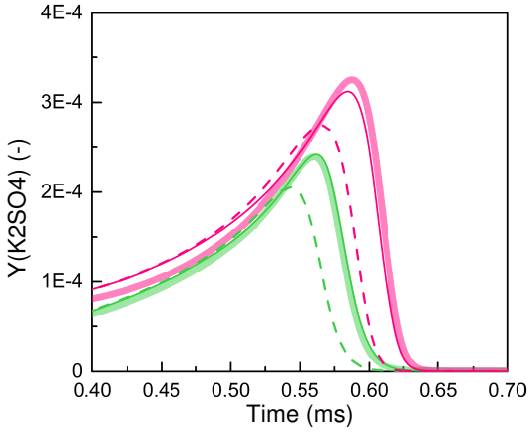


Figure 4: Time evolution of the deterministic mixing trajectories (Eq. 1). K_2SO_4 mass fractions. Green: from oxidizer stream. Pink: fuel stream. Thick solid lines: detailed mechanism [23]. Thin solid lines: reduced mechanism (Table 3). Dashed lines: preliminary reduced mechanism (DRGEP, Table 3 but with original rates parameters)

5). The biomass flame operating conditions are those of [39], where the detailed configurations and numerical methods could be found. The computational domain has physical dimensions of $L_x = L_y = 51.2$ mm. A uniform mesh of $\Delta = 100$ μm is employed, which has been shown to be able to properly resolve the flame structure[46]. Primary air (bulk velocity: 10 m/s, 300 K) laden with 902 pulverized-biomass particles is introduced for $|y| < 2.5$ mm initially, with a hot coflow gas (3 m/s, 1519 K) surrounded. The properties of corn straw (Table 1) is used. The coflow is the burnout gas of corn straw volatile and air at $\phi = 0.45$. Biomass particles' location follows a random uniform distribution and initial particle density is 550 kg/m^3. The particles have a uniform diameter of 25 μm, to fulfill the point-particle assumption and the grid resolution required by DNS. This fine diameter could be achieved with torrefied biomass [47]. Periodic boundary conditions are introduced in all directions. Turbulent fluctuations of 0.05 m/s (0.5% of the primary air velocity) are initially set within the shear layers between the primary jet and the coflow.

The simulations are performed in the Eulerian and Lagrangian frameworks with a low-Mach number in-house code specialized in turbulent solid fuel combustion [34, 39, 46, 48, 49]. The governing equations for the gas and particle phases are those of Wan et al. [39]. Biomass pyrolysis with K/Cl/S release, homogeneous volatile combustion and K/Cl/S reactions are simulated. Heterogeneous char reaction is not considered since its contribution has been shown to be minor in such a small-scale solid fuel flame [33, 49, 50]. The pyrolysis rate of a pulverized-biomass parti-

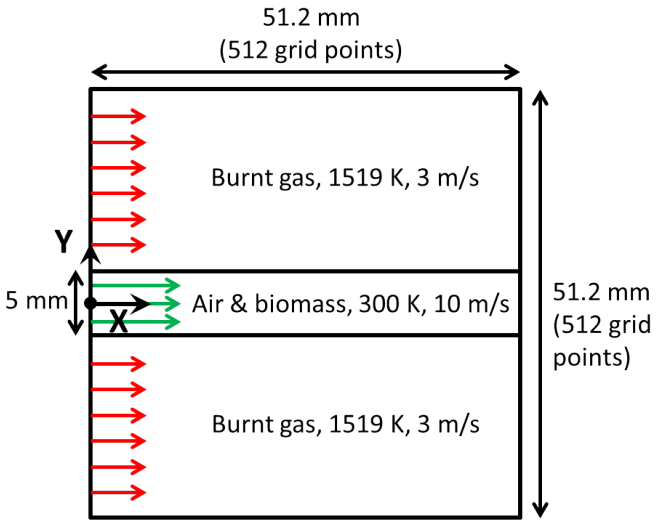


Figure 5: Schematic diagram of computational configuration of the two-dimensional DNS of pulverized-biomass flame.

cle is determined by the single first-order reaction model (SFOM) [51] with its kinetic parameters, i.e., A_v (2.5×10^9 s^{-1}), E_v (11×10^4 J/mol) and Q_v (1.1), calibrated by the bio-CPD model[30], as in [34].

The hydrocarbon volatile combustion is described by the DRM22 skeleton mechanism [29], while the K/Cl/S reactions are simulated with both the detailed [23] and reduced (Table 3) mechanisms. As in previous works[39, 46, 49], the potassium release rate of a biomass particle is set to be proportional to its volatile release rate, because the potassium vapor generated inside the porous structure of a biomass particle will be transported outward by the volatile yielded and the experiments have shown that the alkali release is proportional to the burnout of solid fuel particles during the early combustion stage [20]. Similarly, the release rates of sulfur and chlorine are also set to be proportional to that of the volatile. The detailed composition of the volatile gas is summarized in Table 2.

3.2. Global flame characteristics

The performance of the reduced mechanism in the 2D pulverized-biomass flame is now examined. Figures 6 and 7 show the instantaneous distribution of the gas temperature and particle burnout, and K_2SO_4 mass fraction at five subsequent times. At the early stage of t = 10–15 ms,

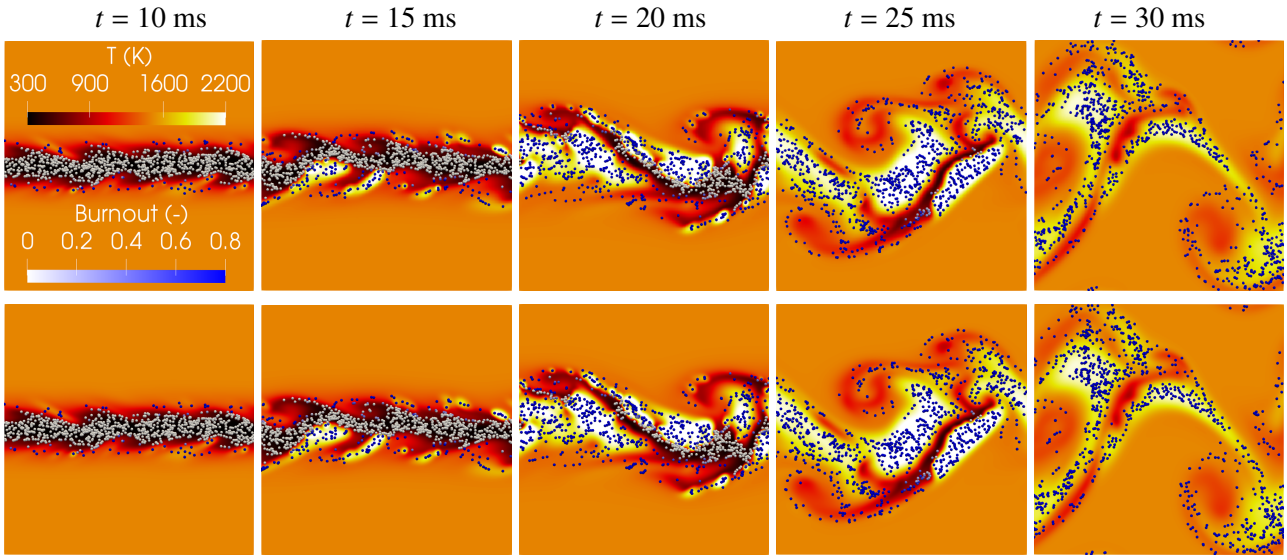


Figure 6: Instantaneous distribution of the gas temperature and particle burnout at subsequent times. Upper: detailed potassium mechanism [23]. Lower: reduced potassium mechanism (Table 3).

biomass particles in the shear layers are firstly heated up by the coflow and then yield volatiles including K/Cl/S species during the pyrolysis process. At t = 20 ms, the heat release from the volatile oxidation is strong enough to ignite adjacent biomass particles, resulting in a rapid spreading flame. The flame in turn heats up surrounding particles and promotes the release of volatile and potassium species KOH, which through potassium reactions forms the zones with a high concentration of K_2SO_4 in Fig. 7. Finally, at t = 30 ms, the flame tends to be weak since most of the biomass particles burn out, while the flame region becomes wider because the turbulent mixing continues. A wide region of high concentration K_2SO_4 can be observed, which means the production of K_2SO_4 is significant. The predictions of the detailed and reduced potassium mechanisms are quite close to each other. Please note although the same DRM22 mechanism is employed for hydrocarbon combustion in both cases, the K/Cl/S reactions interact with the combustion via major species, e.g. O_2, and radicals, e.g., OH.

Figure 8 shows the comparisons between the DNS predictions using the detailed and reduced potassium mechanisms for OH, C_2H_2 and CO_2, and the three major potassium species, KOH, K and KCl at t = 20 ms. The prediction of the reduced potassium mechanism agrees well with that of the detailed mechanism. The good agreement on OH, C_2H_2 and CO_2 between the two cases

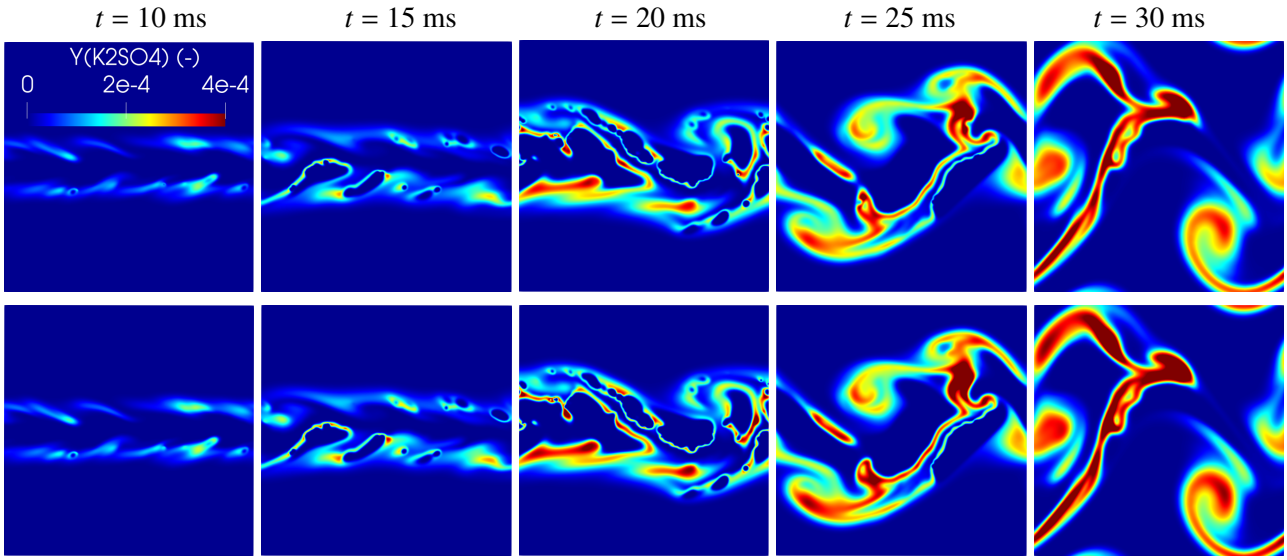


Figure 7: Instantaneous distribution of Na_2SO_4 at subsequent times. Upper: detailed potassium mechanism [23]. Lower: reduced potassium mechanism (Table 3).

indicates the reduction of potassium chemistry does not jeopardize the accuracy of combustion prediction. For the potassium species, it can be observed that the distribution of atomic K closely follows the OH radical distribution, which means the production of atomic K is favored in the regime with strong heat release. High concentration of KOH appears in the region where C_2H_2 accumulates, since both of them are released together during the pyrolysis of biomass particles. KCl also features a high concentration in this region, which can be explained by the reaction between KOH and HCl producing KCl (Reaction R9 in Table 3).

3.3. Quantitative analysis

Figure 9 shows the scatter plots of instantaneous mass fractions of the four major potassium species against the mixture fraction Z predicted by both the detailed and reduced potassium mechanisms at $t = 20$ ms. The data is obtained from every grid point of the entire domain. See also Fig. 10 with $\left(\overline{Y_i|Z^*}\right)$ showing the conditional mixture fraction average and conditional root-mean-square (RMS), $\overline{\left[\left(\overline{Y_i|Z^*}\right) - Y_i \mid Z^*\right]^2}^{1/2}$, of species mass fractions. It can be observed the four major potassium species show different distribution characteristics. Y_{KOH} and Y_{KCl} are increase almost linearly with Z. The distribution of Y_{K} is more subtle. Y_{K} stays close to zero for the range of $Z < 0.1$, to then increase rapidly until $Z = 0.22$, and then keeps an overall increase trend with

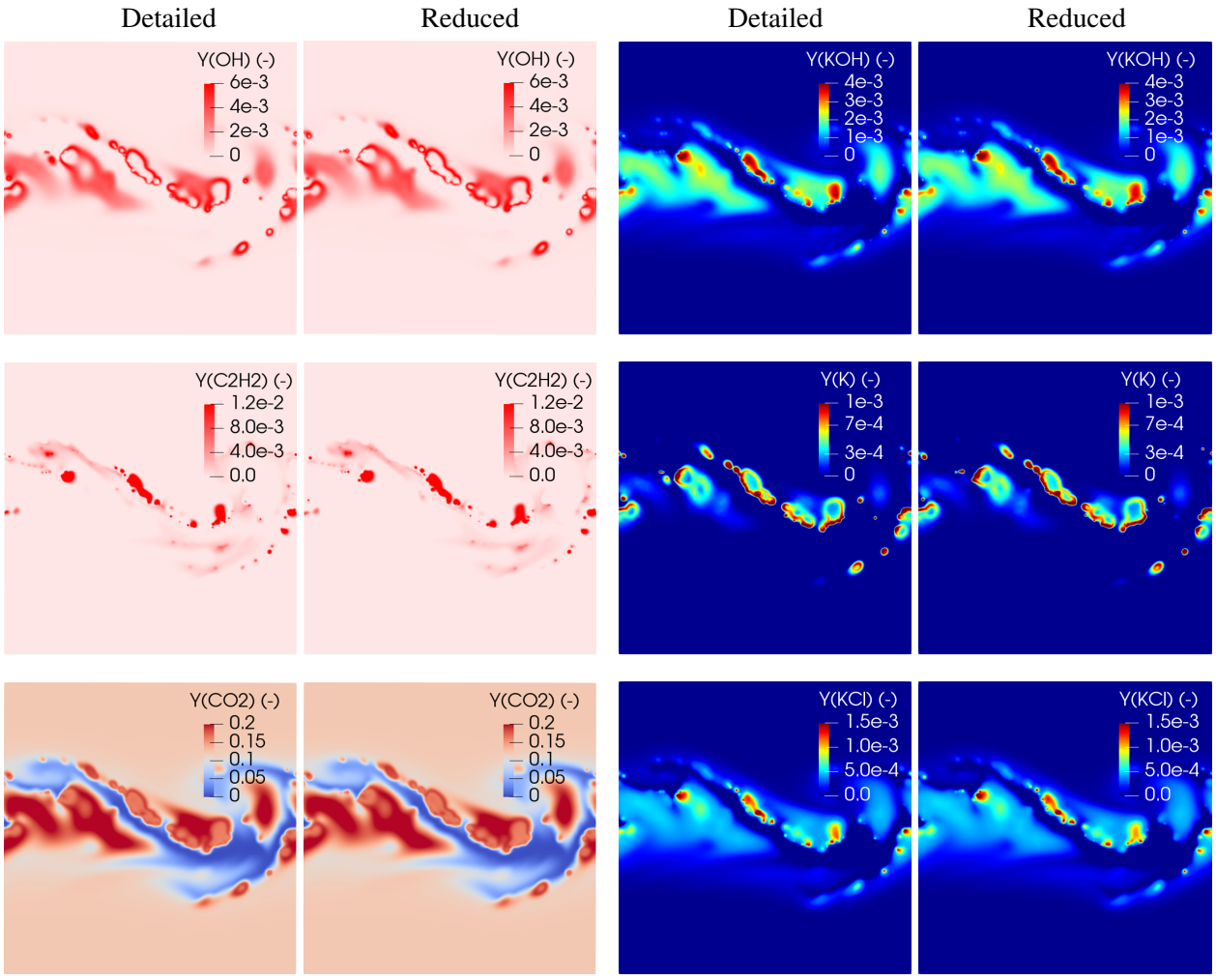


Figure 8: Mass fractions of OH, KOH, C_2H_2, K, CO_2 and KCl at t = 20 ms. Left columns: detailed potassium mechanism [23]. Right columns: reduced potassium mechanism (Table 3)

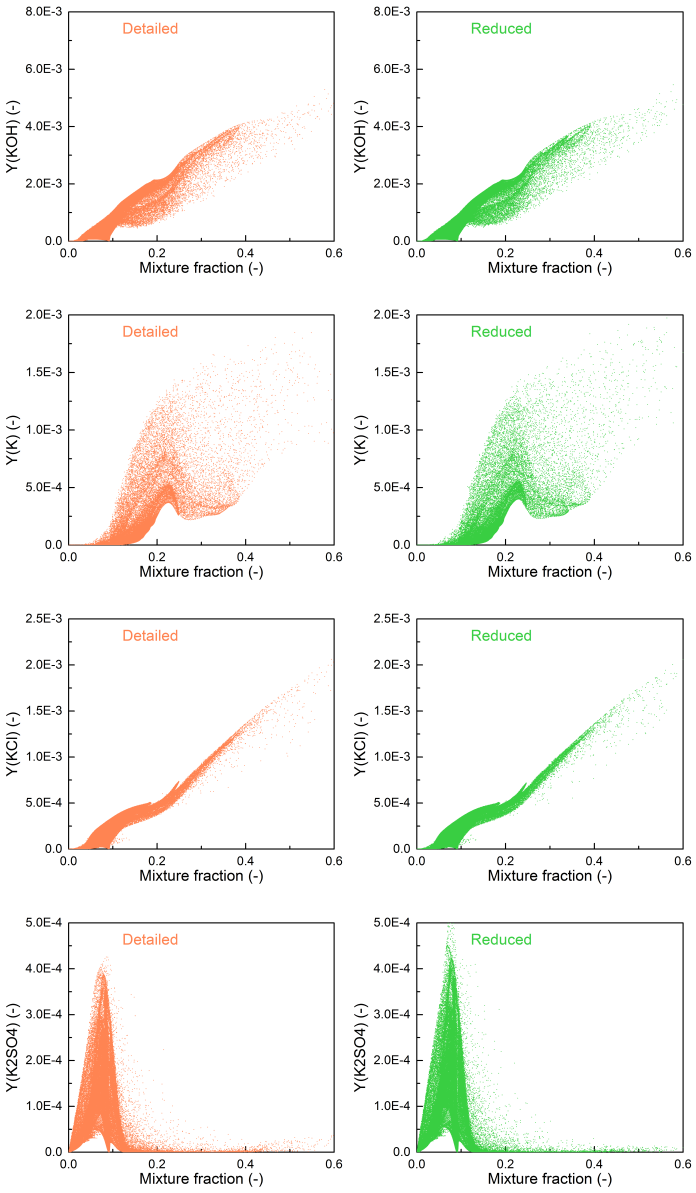


Figure 9: Scatter plots of mass fractions of KOH, K, KCl, K_2SO_4 against mixture fractions at $t = 20$ ms. Left: detailed potassium mechanism [23]. Right: reduced potassium mechanism (Table 3).

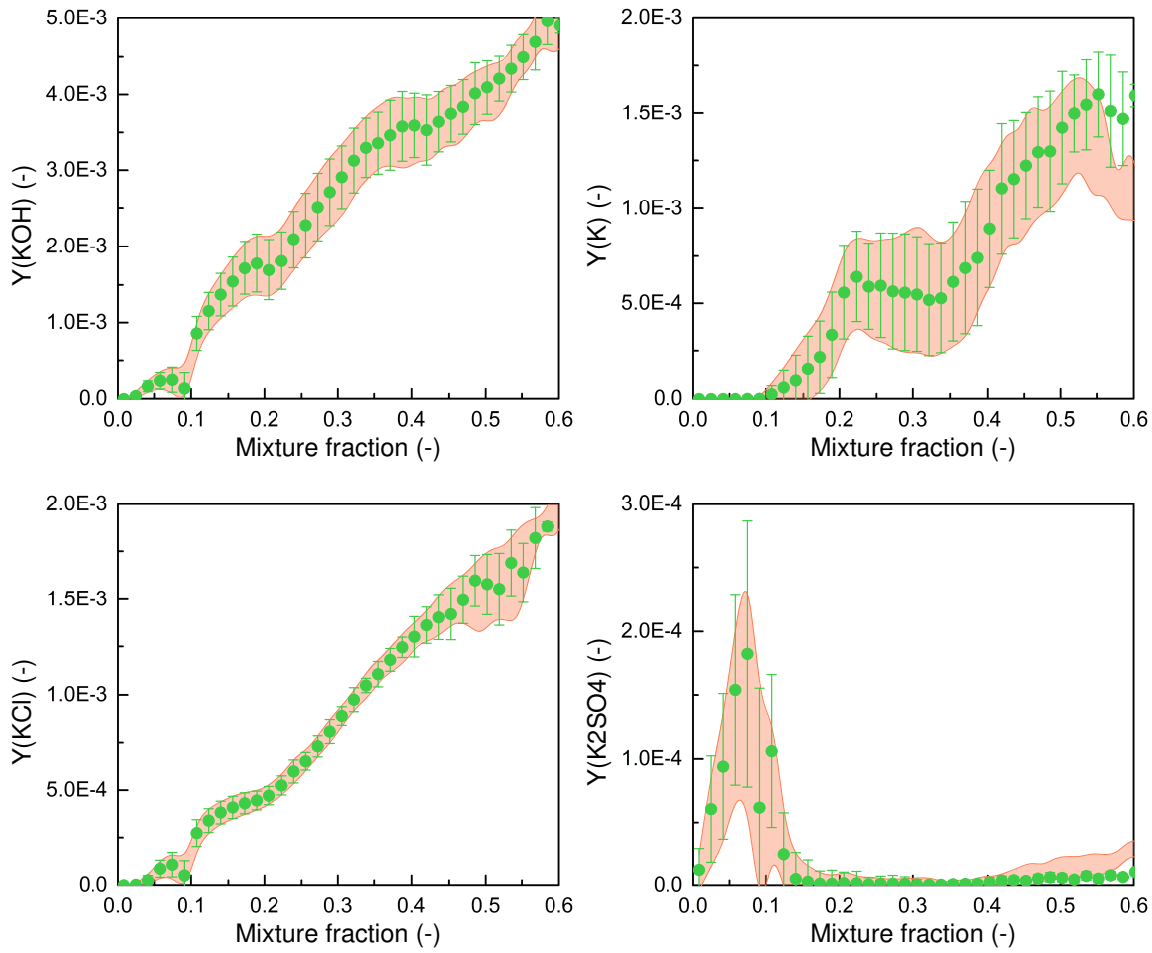


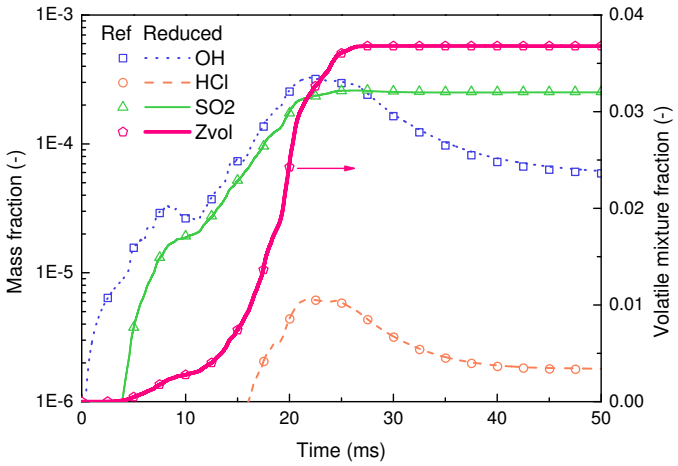
Figure 10: Conditional mixture fraction averages of mass fractions of KOH, K, KCl, K_2SO_4 at t = 20 ms. Range of conditional average ± fluctuation. Orange bands: detailed potassium mechanism [23]. Symbols: reduced potassium mechanism (Table 3).

wide fluctuations in the mixture fraction space. The sulfurous potassium product K_2SO_4 features a single-peak distribution in the fuel-lean regime of $Z < Z_{st} = 0.189$. Due to the influence of the coflow stream (equivalence ratio of 0.45 and $Z = 0.093$) which does not carry potassium species, mass fractions of the four potassium species could reach zero at $Z = 0.093$. The comparison on conditional average and RMS of the potassium species mass fractions (Fig. 10) confirms the accuracy of the reduced potassium mechanism.

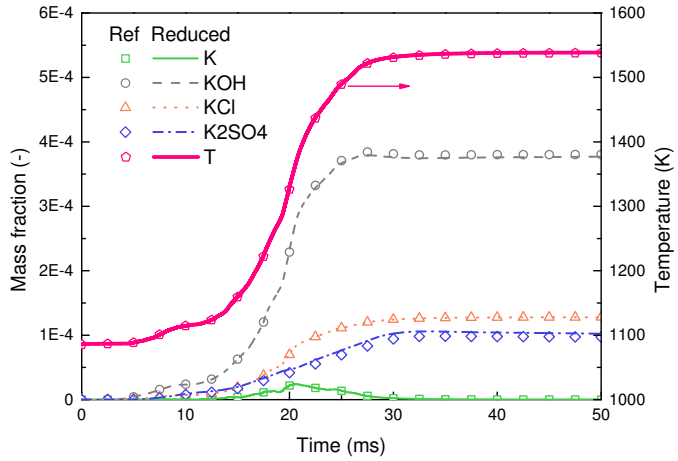
Figure 11 shows the time evolutions of the mass fractions of OH, HCl, SO_2, Z_{vol}, of the four major potassium species and of gas temperature, all of which are averaged over the entire computational domain. Z_{vol} is the volatile mixture fraction, which is a transported scalar with a source term representing the volatile mass released from biomass particles. It can be observed that both the gas temperature and Z_{vol} start to increase around $t = 5$ ms, indicating the first ignition of the biomass jet. During $t \in [15, 20]$ ms, the mass fractions of all the species as well as the gas temperature increase rapidly, which should be attributed to the actively burning of the biomass flame. Both the averaged gas temperature and Z_{vol} become constant after $t = 30$ ms, which means the combustion is completed. Nevertheless, the variance of gas temperature is further decreasing because of the turbulent mixing between the burnout gases and the surroundings, which therefore explains the decreasing of Y_{OH} and Y_{HCl} after $t = 30$ ms. Toward the end of the simulation at $t = 50$ ms, the mass fraction of KCl is higher than that of K_2SO_4. However, the concentration of HCl is an order of magnitude lower than that of SO_2, which indicates that HCl has a much stronger ability to react with potassium species than SO_2. A close agreement between the detailed and reduced potassium mechanisms is reached.

4. Evaluation of the reduced mechanism under different K/Cl/S concentrations

To illustrate the adaptability of of the reduced mechanism to various molar ratio of K/Cl/S in the volatile compositions, a parametric study is performed with different K/Cl/S concentration. As summarized in Table 4, Case A is the original condition employed in the previous Section 3, which is used as the baseline. Cases B, C and D remove the HCl or SO_2, or both of them, from the volatile to explore the performance of the reduced mechanism in the absence of Cl and/or S. Since the content of K in the basline Case A is high for securing the combination with Cl and S to



(a) mass fractions of OH, HCl, SO_2 and Z_{vol}



(b) mass fractions of major sodium species and gas temperature

Figure 11: Time evolutions of the mass fraction of species and volatiles (Z_{vol}) and gas temperature averaged over the computational domain. Symbols: detailed potassium mechanism [23]. Lines: reduced potassium mechanism (Table 3).

Table 4: Simulation cases with different mass fractions of HCl and SO_2 in the volatile compositions. The corresponding molar ratio of K/Cl/S of each case is also illustrated. The reduced part of KOH/HCl/SO_2 is balanced by N_2.

Case	KOH	HCl	SO_2	K/Cl/S molar ratio
A (baseline)	14.7E-3	1.8E-3	8.0E-3	1 / 0.19 / 0.48
B	14.7E-3	0	8.0E-3	1 / 0 / 0.48
C	14.7E-3	1.8E-3	0	1 / 0.19 / 0
D	14.7E-3	0	0	1 / 0 / 0
E	2.76E-3	1.8E-3	1.58E-3	1 / 1 / 0.5
F	2.76E-3	0.9E-3	1.58E-3	1 / 0.5 / 0.5
G	2.76E-3	0.9E-3	8.0E-3	1 / 0.5 / 2.53

form KCl and K_2SO_4, Cases E, F and G are set up to study the response of the reduced mechanism under a lower concentration of potassium.

Each case in Table 4 is simulated twice with both the detailed and reduced potassium mechanisms. Figure 12 shows the time evolutions of the averaged mass fractions of the four major potassium species among Cases A–D of Table 4. It can be observed that the profiles of K are similar among the four cases, which reach a peak value around t = 22 ms and then gradually decrease to negligible concentrations at the end of simulations. When both HCl and SO_2 are removed from the volatile, KOH becomes the only major sodium product at the end of t = 50 ms (Case D). If HCl is removed but SO_2 remains, KOH is then partly transformed to K_2SO_4, with both of them being main potassium products (Case B). Similarly, if SO_2 gets removed but HCl remains, KOH is partly consumed by HCl to generate KCl as another main potassium product (Case C). In all of the Cases A–D, KOH keeps to be the potassium product with highest mass fraction, which indicates the excessive part of potassium tends to form KOH in the post-combustion gases after reacting with Cl and S.

The averaged responses of the four major potassium species in Cases E–G of Table 4 are compared in Fig. 13. The profiles of K are again similar among Cases E–G, which indicates the production of K is barely influenced by Cl and S in the volatiles. In Case E (K:Cl:S = 1:1:0.5), most of the potassium is transformed to KCl while the production of K_2SO_4 is negligible. When the molar ratio of Cl/K decreases to 0.5 in Case F, the formation of KCl is reduced almost by half, with a marginal amount of potassium transformed to K_2SO_4 at the S/K ratio of 0.5. Even though

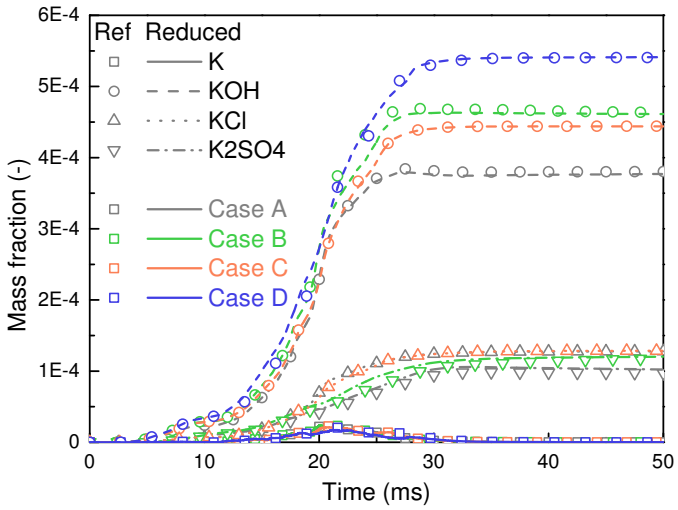


Figure 12: Time evolution of the species mass fractions averaged over the computational domain. Grey: Case A of Table 4. Green: Case B. Orange: Case C. Blue: Case D. Symbols: detailed potassium mechanism [23]. Lines: reduced potassium mechanism (Table 3).

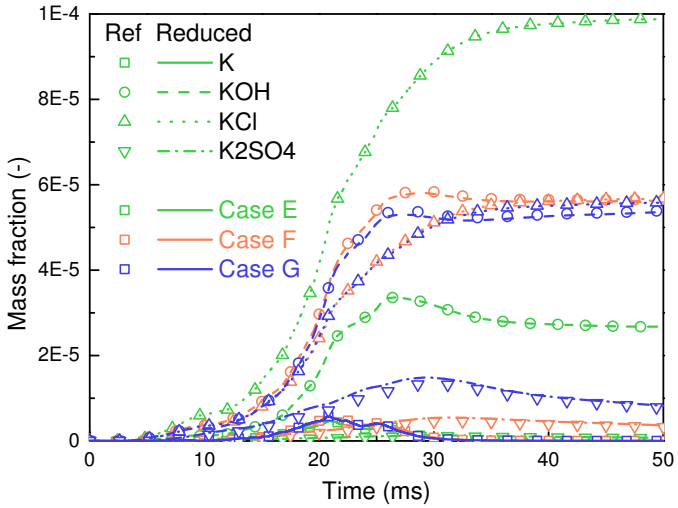


Figure 13: Time evolution of the species mass fractions averaged over the computational domain. Green: Case E of Table 4. Orange: Case F. Blue: Case G. Symbols: detailed potassium mechanism [23]. Lines: reduced potassium mechanism (Table 3).

the S/K ratio is increased to 2.53 in Case G, the formation of K_2SO_4 is still limited ($Y_{K_2SO_4} < 10^{-5}$ at $t = 50$ ms). It should be partly attributed to the lower concentration of potassium in Cases E–G than that in the baseline Case A.

The predictions of the reduced potassium mechanism agree well with that of the detailed one under all different K/Cl/S configurations (Table 4) in the volatile.

These 2D DNS simulations were run over 28 Intel Boardwell cores at 2.4 GHz. The computational cost for the detailed and reduced potassium mechanisms are shown in Fig. 14. To facilitate the comparison, another 2D DNS case was performed without potassium species and reactions, which reflects the CPU cost of hydrocarbon combustion computation. After subtracting this part of CPU cost, the reduced mechanism of Table 3 saves 71.3% of the CPU cost compared to the detailed one.

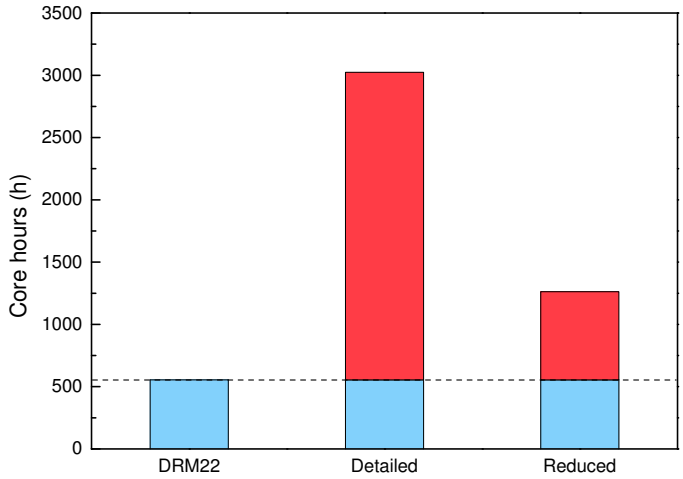


Figure 14: CPU core hours cost of running a 2D DNS case. DRM22: only hydrocarbon combustion is considered with the DRM22 mechanism [29]. Detailed: detailed potassium mechanism [23] is added to simulate potassium chemistry. Reduced: reduced potassium mechanism (Table 3) is added to simulate potassium chemistry.

5. Conclusions

Starting from the detailed potassium mechanism proposed by Glarborg and Marshall [23], an automated reduction and optimization strategy has been employed to develop a reduced mechanism for potassium chemistry during biomass combustion. The reduced mechanism involves 15 K/S/Cl species and 24 elementary reactions. A turbulent non-premixed micro-mixing based canonical problem has been introduced as a reference problem for the mechanism reduction and rates parameters optimization. Then, two-dimensional direct numerical simulations of turbulent pulverized-biomass flames have been performed with both the detailed and the reduced potassium mechanisms. The reduced one achieves a satisfactory prediction on potassium chemistry with a CPU cost reduction reaching up to 71.3%.

The strength of the approach discussed relies on the development of reduced mechanisms in a pre-processing manner, for given operating conditions. In the present work, the reduced potassium mechanism has been developed and validated with the detailed reference mechanism under atmospheric pressure for various K/Cl/S ratio of the volatiles in a non-premixed mixing layer featuring a piloted flame (about 1500 K).

The chemistry reduction focus on the gaseous phase released from the biomass particles. The particle size is chosen according to DNS requirements and it is at the low end of a true particle-size distribution (PSD) for biomass particles. Once the reduced mechanism developed and validated, it should be applicable to a gaseous phase released from biomass particles with a real PSD.

Acknowledgments

This work was jointly supported by the National Natural Science Foundation of China (51706200), Institut Universitaire de France (IUF), the Royal Society and the Engineering and Physical Sciences Research Council (EPSRC) of the UK. Special thanks are due to Prof. Peter Glarborg of DTU, who provided us the detailed mechanism of alkali metal species. Computing resources were provided by CRIANN (`http://www.criann.fr`).

References

[1] H. W. Ryu, D. H. Kim, J. Jae, S. S. Lam, E. D. Park, Y.-K. Park, Recent advances in catalytic co-pyrolysis of biomass and plastic waste for the production of petroleum-like hydrocarbons, Bioresource Technology (2020) 123473.

[2] S. Singh Siwal, Q. Zhang, C. Sun, S. Thakur, V. Kumar Gupta, V. Kumar Thakur, Energy production from steam gasification processes and parameters that contemplate in biomass gasifier A review, Bioresource Technology 297 (2020) 122481.

[3] R. Sankaran, R. A. Parra Cruz, H. Pakalapati, P. L. Show, T. C. Ling, W.-H. Chen, Y. Tao, Recent advances in the pretreatment of microalgal and lignocellulosic biomass: A comprehensive review, Bioresource Technology 298 (2020) 122476.

[4] IEA, Key world energy statistics, Report (2019).

[5] Z. Xue, Z. Zhong, B. Zhang, J. Zhang, X. Xie, Potassium transfer characteristics during co-combustion of rice straw and coal, Applied Thermal Engineering 124 (2017) 1418 – 1424.

[6] F. Li, X. Wang, C. Zhao, Y. Li, M. Guo, H. Fan, Q. Guo, Y. Fang, Influence of additives on potassium retention behaviors during straw combustion: A mechanism study, Bioresource Technology 299 (2020) 122515.

[7] H. Zhang, J. Li, X. Yang, S. Guo, H. Zhan, Y. Zhang, Y. Fang, Influence of coal ash on potassium retention and ash melting characteristics during gasification of corn stalk coke, Bioresource Technology 270 (2018) 416 – 421.

[8] S. Guo, Y. Jiang, Z. Yu, J. Zhao, Y. Fang, Correlating the sodium release with coal compositions during combustion of sodium-rich coals, Fuel 196 (2017) 252–260.

[9] Y. Niu, H. Tan, S. Hui, Ash-related issues during biomass combustion: Alkali-induced slagging, silicate melt-induced slagging (ash fusion), agglomeration, corrosion, ash utilization, and related countermeasures, Progress in Energy and Combustion Science 52 (2016) 1–61.

[10] P. J. van Eyk, P. J. Ashman, Z. T. Alwahabi, G. J. Nathan, The release of water-bound and organic sodium from Loy Yang coal during the combustion of single particles in a flat flame, Combustion and Flame 158 (6) (2011) 1181–1192.

[11] Y. Z. Liu, Z. H. Wang, K. D. Wan, Y. Lv, J. Xia, Y. He, K. F. Cen, In Situ Measurements of the Release Characteristics and Catalytic Effects of Different Chemical Forms of Sodium during Combustion of Zhundong Coal, Energy & Fuels 32 (6) (2018) 6595–6602.

[12] P. E. Mason, J. M. Jones, L. I. Darvell, A. Williams, Gas phase potassium release from a single particle of biomass during high temperature combustion, Proceedings of the Combustion Institute 36 (2) (2017) 2207–2215.

[13] P. E. Mason, L. I. Darvell, J. M. Jones, A. Williams, Observations on the release of gas-phase potassium during the combustion of single particles of biomass, Fuel 182 (2016) 110–117.

[14] W. Weng, M. Costa, M. Aldén, Z. Li, Single particle ignition and combustion of pulverized pine wood, wheat straw, rice husk and grape pomace, Proceedings of the Combustion Institute 37 (3) (2019) 2663–2671.

[15] W. Weng, Q. Gao, Z. Wang, R. Whiddon, Y. He, Z. Li, M. Aldén, K. Cen, Quantitative Measurement of Atomic Potassium in Plumes over Burning Solid Fuels Using Infrared-Diode Laser Spectroscopy, Energy & Fuels 31 (3) (2017) 2831–2837.

[16] T. Sorvajärvi, N. DeMartini, J. Rossi, J. Toivonen, In Situ Measurement Technique for Simultaneous Detection of K, KCl, and KOH Vapors Released during Combustion of Solid Biomass Fuel in a Single Particle Reactor, Applied Spectroscopy 68 (2) (2014) 179–184.

[17] Y. Z. Liu, Z. H. Wang, J. Xia, L. Vervisch, K. D. Wan, Y. He, R. Whiddon, H. Bahai, K. F. Cen, Measurement and kinetics of elemental and atomic potassium release from a burning biomass pellet, Proceedings of the Combustion Institute 37 (3) (2019) 2681–2688.

[18] W. Weng, S. Li, M. Costa, Z. Li, Quantitative imaging of potassium release from single burning pulverized biomass char particles, Fuel 264 (2020) 116866.

[19] Z.-h. Zhang, Q. Song, Z. T. Alwahabi, Q. Yao, G. J. Nathan, Temporal release of potassium from pinewood particles during combustion, Combustion and Flame 162 (2) (2015) 496–505.

[20] Y. Z. Liu, Y. He, Z. H. Wang, K. D. Wan, J. Xia, J. Z. Liu, K. F. Cen, Multi-point LIBS measurement and kinetics modeling of sodium release from a burning Zhundong coal particle, Combustion and Flame 189 (2018) 77–86.

[21] S. Srinivasachar, J. J. Helble, D. O. Ham, G. Domazetis, A kinetic description of vapor phase alkali transformations in combustion systems, Progress in Energy and Combustion Science 16 (4) (1990) 303–309.

[22] M. Steinberg, K. Schofield, The chemistry of sodium with sulfur in flames, Progress in Energy and Combustion Science 16 (4) (1990) 311–317.

[23] P. Glarborg, P. Marshall, Mechanism and modeling of the formation of gaseous alkali sulfates, Combustion and Flame 141 (1–2) (2005) 22–39.

[24] K. Iisa, Y. Lu, K. Salmenoja, Sulfation of Potassium Chloride at Combustion Conditions, Energy & Fuels 13 (6) (1999) 1184–1190.

[25] S. Akbar, U. Schnell, G. Scheffknecht, Modelling potassium release and the effect of potassium chloride on deposition mechanisms for coal and biomass-fired boilers, Combustion Theory and Modelling 14 (3) (2010) 315–329.

[26] M. U. Garba, D. B. Ingham, L. Ma, R. T. J. Porter, M. Pourkashnian, H. Z. Tan, A. Williams, Prediction of Potassium Chloride Sulfation and Its Effect on Deposition in Biomass-Fired Boilers, Energy & Fuels 26 (11) (2012) 6501–6508.

[27] N. Jaouen, L. Vervisch, P. Domingo, G. Ribert, Automatic reduction and optimisation of chemistry for turbulent combustion modelling: Impact of the canonical problem, Combustion and Flame 175 (2017) 60–79.

[28] N. Jaouen, L. Vervisch, P. Domingo, Auto-thermal reforming (ATR) of natural gas: An automated derivation of optimised reduced chemical schemes, Proceedings of the Combustion Institute 36 (3) (2017) 3321 – 3330.

[29] A. Kazakov, M. Frenklach, Reduced reaction sets based on GRI-Mech 1.2 (1994).
URL `http://www.me.berkeley.edu/drm/`

[30] C. D. Sheng, J. L. T. Azevedo, Modeling biomass devolatilization using the chemical percolation devolatilization model for the main components, Proceedings of the Combustion Institute 29 (2002) 407–414.

[31] K. D. Wan, Z. H. Wang, Y. He, J. Xia, Z. J. Zhou, J. H. Zhou, K. F. Cen, Experimental and modeling study of pyrolysis of coal, biomass and blended coal–biomass particles, Fuel 139 (2015) 356–364.

[32] Z. H. Wang, K. D. Wan, J. Xia, Y. He, Y. Z. Liu, J. Z. Liu, Pyrolysis Characteristics of Coal, Biomass, and Coal–Biomass Blends under High Heating Rate Conditions: Effects of Particle Diameter, Fuel Type, and Mixing Conditions, Energy & Fuels 29 (8) (2015) 5036–5046.

[33] M. Rieth, A. G. Clements, M. Rabaçal, F. Proch, O. T. Stein, A. M. Kempf, Flamelet LES modeling of coal combustion with detailed devolatilization by directly coupled CPD, Proceedings of the Combustion Institute 36 (2) (2017) 2181–2189.

[34] K. D. Wan, J. Xia, Z. H. Wang, L. C. Wrobel, K. F. Cen, Online-CPD-coupled large-eddy simulation of pulverized-coal pyrolysis in a hot turbulent nitrogen jet, Combustion Science and Technology 189 (1) (2017) 103–131.

[35] T. Takuwa, I. Naruse, Emission control of sodium compounds and their formation mechanisms during coal combustion, Proceedings of the Combustion Institute 31 II (2007) 2863–2870.

[36] C. Dopazo, E. E. O'Brien, Functional formulation of nonisothermal turbulent reactive flows, The Physics of Fluids 17 (11) (1974) 1968–1975.

[37] R. Borghi, Turbulent combustion modelling, Progress in Energy and Combustion Science 14 (4) (1988) 245–292.

[38] R. L. Curl, Dispersed phase mixing: I. Theory and effects in simple reactors, AIChE Journal 9 (2) (1963) 175–181.

[39] K. Wan, Z. Wang, J. Xia, L. Vervisch, P. Domingo, Y. Lv, Y. Liu, Y. He, K. Cen, Numerical study of HCl and SO2 impact on potassium emissions in pulverized-biomass combustion, Fuel Processing Technology 193 (2019) 19 – 30.

[40] K. Bioche, G. Ribert, L. Vervisch, Simulating upstream flame propagation in a narrow channel after wall preheating: Flame analysis and chemistry reduction strategy, Combustion and Flame 200 (2019) 219 – 231.

[41] C. Locci, L. Vervisch, B. Farcy, P. Domingo, N. Perret, Selective Non-catalytic Reduction (SNCR) of Nitrogen Oxide Emissions: A Perspective from Numerical Modeling, Flow, Turbulence and Combustion 100 (2) (2018) 301–340.

[42] D. G. Goodwin, R. L. Speth, H. K. Moffat, B. W. Weber, Cantera: An Object-oriented Software Toolkit for Chemical Kinetics, Thermodynamics, and Transport Processes, `https://www.cantera.org`, version 2.4.0 (2018).

[43] T. Lu, C. K. Law, A directed relation graph method for mechanism reduction, Proceedings of the Combustion Institute 30 (1) (2005) 1333 – 1341.

[44] P. Pepiot-Desjardins, H. Pitsch, An efficient error-propagation-based reduction method for large chemical kinetic mechanisms, Combustion and Flame 154 (1) (2008) 67 – 81.

[45] J. H. Holland, Adaptation in Natural and Artificial Systems: An Introductory Analysis with Applications to Biology, Control and Artificial Intelligence, MIT Press, Cambridge, MA, USA, 1992.

[46] K. D. Wan, L. Vervisch, J. Xia, P. Domingo, Z. H. Wang, Y. Z. Liu, K. F. Cen, Alkali metal emissions in an early-stage pulverized-coal flame: DNS analysis of reacting layers and chemistry tabulation, Proceedings of the Combustion Institute 37 (3) (2019) 2791–2799.

[47] J. Li, E. Biagini, W. Yang, L. Tognotti, W. Blasiak, Flame characteristics of pulverized torrefied-biomass combusted with high-temperature air, Combustion and Flame 160 (11) (2013) 2585–2594.

[48] K. D. Wan, J. Xia, Z. H. Wang, M. Pourkashanian, K. F. Cen, Large-eddy Simulation of Pilot-assisted

Pulverized-coal Combustion in a Weakly Turbulent Jet, Flow, Turbulence and Combustion 99 (2) (2017) 531–550.

[49] K. D. Wan, J. Xia, L. Vervisch, Y. Z. Liu, Z. H. Wang, K. F. Cen, Modelling alkali metal emissions in large-eddy simulation of a preheated pulverised-coal turbulent jet flame using tabulated chemistry, Combustion Theory and Modelling 22 (2) (2018) 203–236.

[50] R. Knappstein, G. Kuenne, A. Ketelheun, J. Köser, L. Becker, S. Heuer, M. Schiemann, V. Scherer, A. Dreizler, A. Sadiki, J. Janicka, Devolatilization and volatiles reaction of individual coal particles in the context of FGM tabulated chemistry, Combustion and Flame 169 (2016) 72–84.

[51] S. Badzioch, P. G. W. Hawksley, Kinetics of thermal decomposition of pulverized coal particles, Industrial & Engineering Chemistry Process Design and Development 9 (4) (1970) 521–530.